Scientific Research Publishing

Journal of Biosciences and Medicines, 2025, 13(1), 230-242
https://www.scirp.org/journal/jbm
ISSN Online: 2327-509X
ISSN Print: 2327-5081

Changes in the Mechanical Environment of the Nucleus with Cell Crowding and Its Effects on DNA Damage Resistance

Kazuaki Nagayama, Yuto Hirooka

Micro-Nano Biomechanics Laboratory, Department of Mechanical Systems Engineering, Ibaraki University, Ibaraki, Japan
Email: kazuaki.nagayama.bio@vc.ibaraki.ac.jp

How to cite this paper: Nagayama, K. and Hirooka, Y. (2025) Changes in the Mechanical Environment of the Nucleus with Cell Crowding and Its Effects on DNA Damage Resistance. *Journal of Biosciences and Medicines*, **13**, 230-242.
https://doi.org/10.4236/jbm.2025.131019

Received: December 16, 2024
Accepted: January 18, 2025
Published: January 21, 2025

Abstract

Nuclear DNA, which is essential for the transmission of genetic information, is constantly damaged by external stresses and is subsequently repaired by the removal of the damaged region, followed by resynthesis of the excised region. Accumulation of DNA damage with failure of repair processes leads to fatal diseases such as cancer. Recent studies have suggested that intra- and extranuclear environments play essential roles in DNA damage. However, numerous questions regarding the role of the nuclear mechanical environment in DNA damage remain unanswered. In this study, we investigated the effects of cell confluency (cell crowding) on the morphology of cell nuclei, and cytoskeletal structures, and DNA damage in NIH3T3 skin fibroblasts and HeLa cervical cancer cells. Although nuclear downsizing was observed in both NIH3T3 and HeLa cells with cell crowding, intracellular mechanical changes in the two cell types displayed opposite tendencies. Cell crowding in NIH3T3 cells induced reinforcement of actin filament structures, cell stiffening, and nuclear downsizing, resulting in a significant decrease in endogenous DNA damage, whereas cell crowding in HeLa cells caused partial depolymerization of actin filaments and cell softening, inducing endogenous DNA damage. Ultraviolet (UV) radiation significantly increased DNA damage in NIH3T3; however, this response did not change with cell crowding. In contrast, UV radiation did not cause DNA damage in HeLa cells under either sparse or confluent conditions. These results suggested that cell crowding significantly influenced endogenous DNA damage in cells and was quite different in NIH3T3 and HeLa cells. However, cell crowding did not affect the UV-induced DNA damage in either cell type.

Keywords

Cell Biomechanics, Mechanobiology, Mechanical Properties, DNA Damage,

γ-H2A.X

1. Introduction

Nuclear DNA, which is essential for the transmission of genetic instructions, is constantly damaged by external stresses, such as ultraviolet (UV) radiation, and cells have a self-repair mechanism for DNA damage. However, chronic exposure to such stresses disrupts damage repair mechanisms, resulting in the accumulation of DNA damage and leading to fatal diseases such as cancer [1]. Many studies have been conducted in the fields of biology and medical engineering to elucidate the mechanisms underlying DNA damage and repair [2] [3].

It was recently reported that the mechanical or physical environment of the nucleus can affect the regulation of DNA damage and repair. Takata *et al.* [4] used isolated cell nuclei to demonstrate that DNA double-strand breaks after exposure to ionizing radiation were significantly lower in condensed DNA than in decondensed DNA. Shen *et al.* [5] found that the nuclei of cells migrating through tissues were greatly compressed, resulting in a significant accumulation of DNA damage. We have also investigated the effects of mechanical stimuli and nuclear deformation on the UV radiation resistance of intranuclear DNA and found that UV-induced nuclear DNA damage could be markedly suppressed in cells whose nuclei were largely deformed by cyclic mechanical stretch stimulation [6] or by mechanical trapping by the surface microstructures of culture substrates, such as an array of micropillars [7] [8].

The shape and size of the nucleus, which are deeply involved in the intra- and extra-mechanical environments of the nucleus, are influenced by the cell-cell interactions due to cell density changes [9]. Cell density also affects various cellular functions such as cell proliferation and motility [10] [11], and high-density cultured cancer cells exhibit marked DNA damage [12]. These reports imply that cell-cell mechanical interactions due to cell density changes affect intranuclear DNA damage and repair processes; however, none of the studies have examined cell-type differences in cell crowding-dependent DNA damage and DNA damage resistance, especially while taking into account changes in the mechanical environment of the cell nucleus.

In this study, we investigated the effects of cell density on the mechanical environment of the cell nucleus and cellular DNA damage resistance. Using confocal fluorescence microscopy and atomic force microscopy (AFM), we assessed cell crowding-induced morphological and mechanical changes in the nucleus and intranuclear DNA damage in NIH3T3 skin fibroblasts and cervical cancer HeLa cells, which are widely used to investigate cell type-dependent differences in responses [13]-[15]. We also examined differences in UV-induced DNA damage resistance between the two cell types.

2. Materials and Methods

2.1. Preparation of Specimen Cells

A mouse skin fibroblast cell line (NIH3T3 cells, RIKEN BRC) was used as a normal cell line, and a human cervical cancer cell line (HeLa cells, RIKEN BRC) was used for comparison. The cells were cultured in Dulbecco's Modified Eagle's medium (Wako) supplemented with 10% fetal bovine serum (CELLect Gold), penicillin (100 units/ml), and streptomycin (100 μg/ml; Sigma) in a 5% CO_2 incubator at 37˚C with approximately 100% humidity. For the experiments, cells with different seeding densities were prepared for both cell types according to previous studies [12]: sparse group (SPG, 20 cells/mm^2) and fully confluent group (CFG, 200 cells/mm^2). These cells were seeded onto uncoated φ35-mm glass-bottomed culture dishes (D11140H, Matsunami) and cultured for 48 h for complete spreading.

2.2. Actin Filaments and DNA Staining and Cell Morphological Analysis

The cells were fixed in 10% neutral-buffered formalin for 10 min, permeabilized with PBS containing 0.5% Triton X-100 (ICN Biomedicals, Irvine, CA) for 5 min, and rinsed with PBS containing 1% bovine serum albumin (BSA; Sigma) to block nonspecific protein binding. Actin filaments in the cells were fluorescently stained after incubation with Alexa Fluor 488-conjugated phalloidin (1/300, Molecular Probes) at a concentration of approximately 200 nM for 60 min. Nuclear DNA was fluorescently labeled with Hoechst 33342 (1/1000, Molecular Probes) for 60 min.

The stained cells were placed on the stage of an inverted fluorescence microscope (IX71, Olympus) equipped with a motorized XYZ stage (ProScan, Prior), confocal system (CSU-X1; Yokogawa, Tokyo, Japan), multicolor fluorescence system (Light Engine Spectra-X; OPTO-LINE, Tokyo, Japan), and digital complementary metal-oxide semiconductor (CMOS) camera (ORCA-Flash4.0 V2; Hamamatsu Photonics, Hamamatsu, Japan). The cells were observed using a 60x oil immersion objective lens (UPLSAPO 60XO, NA = 1.35, Olympus). Confocal images were acquired at 0.5 μm intervals in the thickness range of the cells (10 - 15 μm). Nuclear area, nuclear volume (volume of nuclear DNA stained with Hoechst 33342), and nuclear shape index (*SI*) were measured from additional projection images. *SI* expressed by Equation (1), is defined as 1.0 for a circle and approaches zero for highly elongated shapes.

$$SI = \frac{4\pi A}{P^2} \tag{1}$$

where A and P are the projected area and perimeter of the nucleus, respectively.

2.3. DNA Damage Staining

Intranuclear DNA damage in cells was detected using phosphohistone 2AX (γ-

H2A.X), a major marker of DNA double-strand breaks, with immunofluorescence staining. Cells were fixed, permeabilized, and blocked for nonspecific protein binding using the procedure described in the previous section. The cells were incubated with mouse antibodies against γ-H2A.X (1:200 dilution, Anti-gamma H2A.X [ab81299]; Abcam) for 1 h at room temperature (25˚C). After primary incubation, the cells were incubated with a secondary antibody (goat anti-mouse Alexa Fluor 546 [1:200 dilution; Invitrogen]) for 1 h at room temperature. All antibodies were diluted in PBS containing 1% BSA. Intranuclear DNA was stained with Hoechst 33342 as described above. Confocal fluorescence image slices of the stained cells were captured using an inverted fluorescence microscope and confocal system as described above. To assess cellular DNA damage, a projection image was created using the image slices within the thickness range of the nucleus.

2.4. UV Radiation and DNA Damage Analysis

To examine the effects of cell density or cell-type differences on UV-induced DNA damage resistance, the SPG and CFG in both NIH3T3 and HeLa cells, prepared as described in Section 2.1, were exposed to UV radiation of approximately 4.5 mW/cm^2 for 20 s using a conventional UV germicidal lamp with a peak emission at 254 nm, which is based on those of previous studies [8]. The damage caused by UV radiation was evaluated by the expression level of γ-H2A.X 40 min after UV radiation, because the peak expression of γ-H2A.X was reported to be 30 min to 1 h after UV radiation [16].

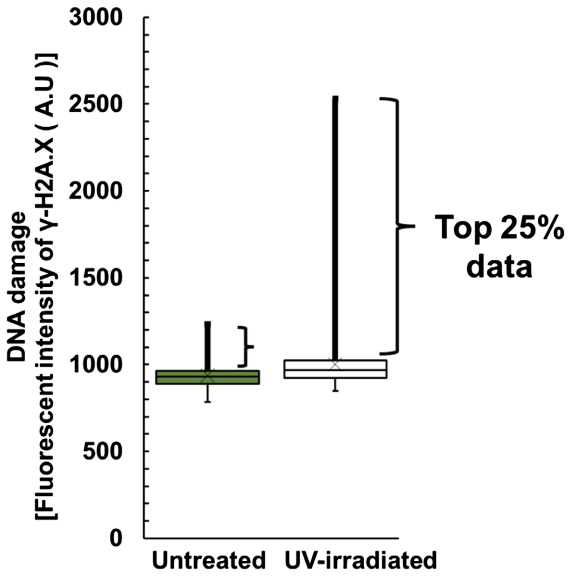

Figure 1. Representation of box plots for fluorescent intensity of γ-H2A.X (DNA damage). The top 25% of the data in the UV-radiated group are defined as UV-radiated DNA damage.

The fluorescent intensity of Hoechst-stained DNA and γ-H2A.X was measured on the same pixel in the confocal fluorescence projection image of nucleus. γ-

H2A.X is slightly expressed even before UV radiation (endogenous DNA damage due to DNA replication stress, etc.); therefore, it is necessary to classify "UV radiation-induced γ-H2A.X" accurately. In a preliminary experiment, we analyzed the range of γ-H2A.X fluorescence in the UV-radiated and control (non-radiated) groups using box and whisker plots (**Figure 1**). The fluorescent intensity of γ-H2A.X in the control group was approximately 1000, whereas that in the UV-radiated group ranged from 1000 to 2500, with a wide variation. Thus, we extracted the top 25% of the fluorescent intensity data from both the control and UV-radiated groups and calculated the mean values and standard deviations.

2.5. Analysis of Cell Surface Topography and Elastic Modulus Using Atomic Force Microscopy (AFM)

To estimate the mechanical environment around the cell nucleus associated with cell crowding, the surface topography and surface elastic modulus of the cells were measured using AFM (NanoWizard IV, JPK Instruments-AG) mounted on top of an inverted optical microscope (IX73, Olympus, Japan) equipped with a digital CMOS camera (Zyla, Andor). The nuclei of the cells were fluorescently visualized with low-concentration Hoechst 33342. Phase-contrast images of the cells and fluorescent images of the nuclei were captured with the AFM-equipped CMOS camera using a 20x objective lens (PhC, NA = 0.4, Olympus) to accurately identify the nuclear region of the cells.

AFM quantitative imaging (QI) mode was used to obtain a force-displacement curve at each pixel of 128 × 128 pixels (100 × 100 μm of measured area) by a precisely controlled high-speed indentation test using rectangular-shaped silicon nitride cantilevers with a cone probe (BioLever-mini, BL-AC40TS-C2; Olympus, Japan) at a spring constant of 0.08 - 0.10 N/m and a nominal tip radius of 10 nm. QI mode measurements were performed within 1 h of transferring the specimen to AFM. These high-speed indentations were performed until a pre-set force of 1 nN was attained. This typically corresponded to cell indentation depths of 200 - 300 nm. Cell elasticity was calculated from the obtained force-displacement curves by applying the Hertzian model (Hertz 1881), which approximates the sample to be isotropic and linearly elastic. Young's (elastic) modulus can be extracted by fitting all force-displacement curves with the following Hertzian model approximation:

$$F = \frac{2E \cdot \tan\alpha}{\pi\left(1-\nu^2\right)}\delta^2 \tag{2}$$

where F is the applied force, E is the elastic modulus, ν is Poisson's ratio (0.5 for a non-compressible biological sample), α is the opening angle of the cone of the cantilever tip, and δ is the indentation depth of the sample recorded in the force-displacement curves. Using the results of the Hertzian model approximation, we identified the Z contact points (specimen surface) and elastic modulus of the specimens at each pixel and produced a surface topography map and elastic modulus map of the specimens.

2.6. Statistical Analysis

Data are expressed as means ± standard deviation (SD). Statistical significance was assessed using the Student's paired and unpaired *t*-test with the statistical analysis program MEPHAS (https://alain003.phs.osaka-u.ac.jp/mephas/). A significance level of $P < 0.05$ was used for all analyses.

3. Results

First, we investigated cell density-dependent morphological changes in the nuclei and actin filaments of NIH3T3 and HeLa cells. Under sparse conditions, NIH3T3 cells had a stellate morphology with a curved periphery and actin filaments localized only in the cell periphery (Figure 2(A)), whereas HeLa cells had a polygonal morphology with relatively clear actin filaments in the central region of the cells (Figure 2(B)). In the confluent state with cell crowding, cells attached to each other and formed mature tissues in both NIH3T3 and HeLa cells (Figure 2(C), Figure 2(D)). NIH3T3 cells displayed thick bundles of actin stress fibers around the nucleus (Figure 2(C)), whereas in HeLa cells, actin filaments were partially depolymerized (Figure 2(D)).

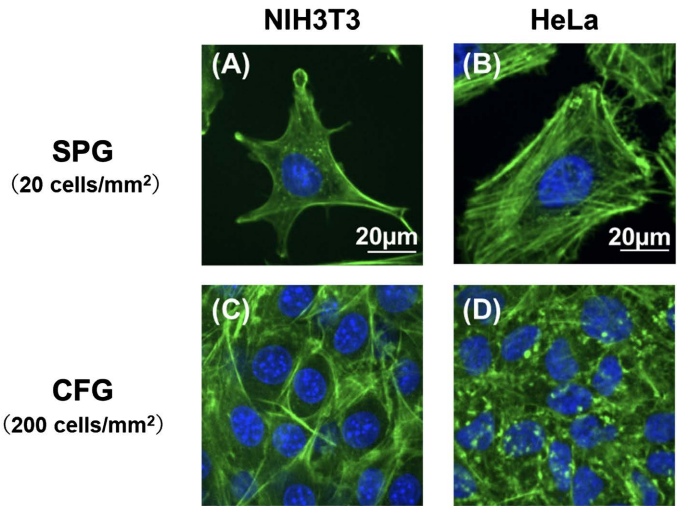

Figure 2. Typical examples of fluorescence images of DNA (blue) and actin filaments (green) of NIH3T3 cells ((A), (C)) and HeLa cells ((B), (D)) in sparse ((A), (B): SPG) and confluent ((C), (D): CFG) culture conditions. In cell crowding (confluent), reinforcement of actin filament structures was observed in NIH3T3 cells (C), but actin filaments were partially broken in HeLa cells (D).

Analysis of the nuclear morphology and Hoechst-stained DNA fluorescence intensity revealed that the nuclear projected area and volume of both cell types significantly decreased with cell crowding (Figure 3(A), Figure 3(B), Figure 3(E), Figure 3(F)), and the nuclear volume decrease was pronounced in the confluent HeLa cells (Figure 3(F)). Nuclear *SI* in both cell types did not change significantly with cell crowding (Figure 3(C), Figure 3(G)). The fluorescence intensity of Hoechst-stained DNA, which is an index of intranuclear DNA accumulation, did

not change with cell crowding in NIH3T3 cells (Figure 3(D)). In contrast, it increased by approximately 20% in HeLa cells (Figure 3(H)), indicating DNA accumulation, possibly due to a pronounced decrease in nuclear volume with HeLa cell crowding (Figure 3(F)).

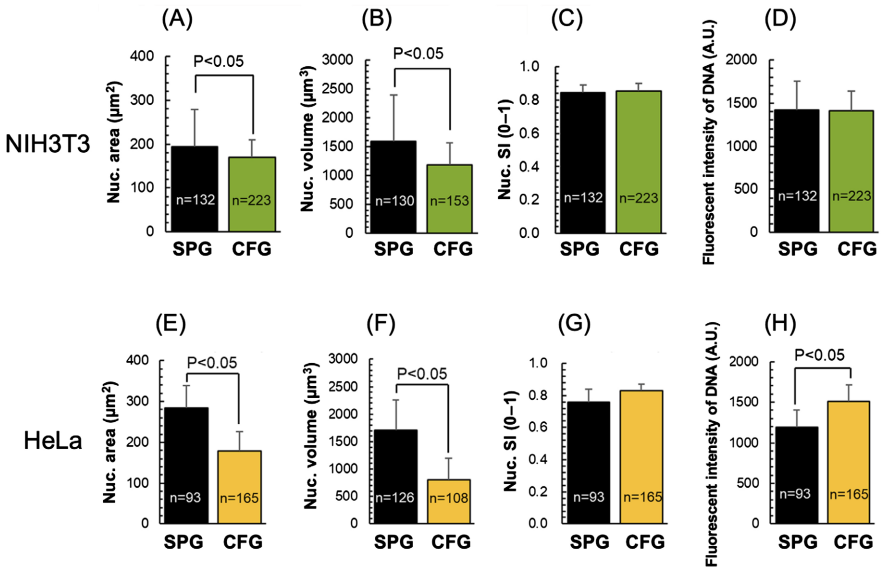

Figure 3. Differences in the nuclear morphology and fluorescent intensity of intranuclear DNA of NIH3T3 ((A)-(D)) and HeLa ((E)-(H)) cells cultured under sparse (SPG) and confluent (CFG) conditions. Mean + SD. N = number of analyzed cells.

Figure 4 shows a representative example of cell surface topography maps and elastic modulus maps obtained by the AFM QI mode with a high-speed indentation test and the quantitative results of the cell surface elastic modulus. Under sparse conditions, both NIH3T3 and HeLa cells had relatively smooth surfaces with rounded elevations in the nuclear region (Figure 4(A), Figure 4(E)). The surface elastic modulus map of NIH3T3 cells was almost uniform over the entire cell surface (Figure 4(C)), indicating homogeneous mechanical properties, whereas sparse HeLa cells showed a fiber-like distribution with a high elastic modulus at the cell periphery and around the nucleus (Figure 4(G), red arrowheads). Under confluent conditions, both cell types displayed a more dome-like surface shape with dense cell tissue, but the change in their surface stiffness showed the opposite trend: the surface elastic modulus of NIH3T3 cells significantly increased with cell crowding (Figure 4(I), Figure 4(J)), especially at the cell body, which was approximately 10 times higher than that of the sparse condition (Figure 4(J)). In contrast, the surface elastic modulus of HeLa cells decreased slightly with cell crowding, both in the cell body and in the nuclear region, but no significant difference was observed (Figure 4(K), Figure 4(L)).

Finally, we investigated the changes in DNA damage and resistance to UV radiation in NIH3T3 and HeLa cells by analyzing the fluorescent intensity of γ-H2A.X (Figure 5). In the untreated control condition, γ-H2A.X was randomly

scattered in the intranuclear spaces of both cell types as "foci" (Figure 5(A), Figure 5(E)), which may represent the endogenous damage of DNA due to constantly occurring physiological DNA replication. This endogenous damage tended to be lower in sparse HeLa cells than in sparse NIH3T3 cells (compare Figure 5(I), Figure 5(J), black bars). The expression of γ-H2A.X foci was altered by cell crowding and was different in both cell types (Figure 5(B), Figure 5(F)). The expression of γ-H2A.X significantly decreased by approximately 15% with cell crowding in NIH3T3 cells (Figure 5(I), compare black and green bars), whereas it increased significantly with cell crowding in HeLa cells (Figure 5(J), compare black and yellow bars). The fluorescent intensity values of γ-H2A.X significantly increased in NIH3T3 cells after UV radiation, regardless of the cell density (Figure 5(C), Figure 5(D), Figure 5(I)). In contrast, the intensity values significantly decreased in HeLa cells under both sparse and confluent conditions after UV radiation (Figure 5(G), Figure 5(H), Figure 5(J)).

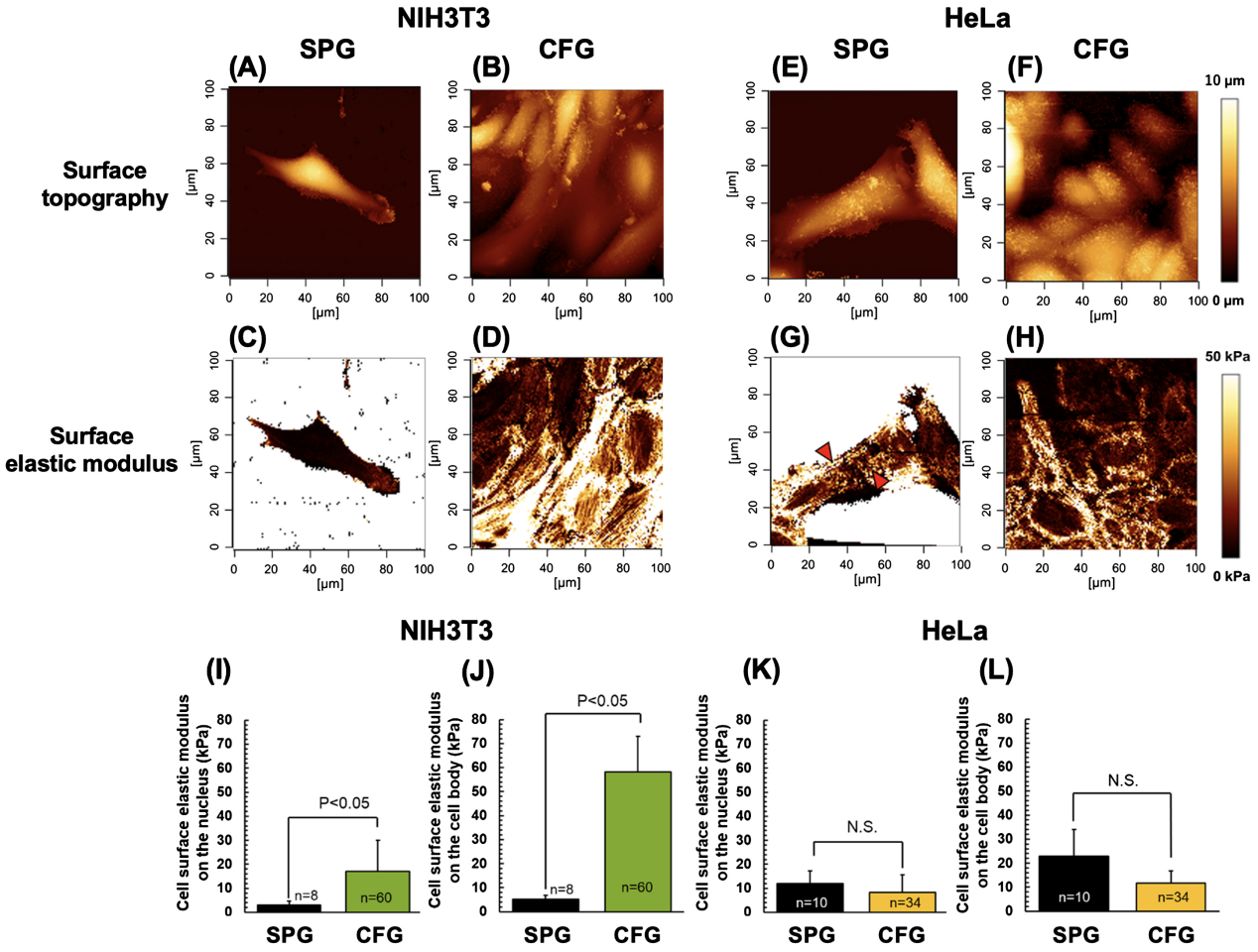

Figure 4. Atomic force microscopy (AFM) images of NIH3T3 ((A)-(D)) and HeLa cells ((E)-(H)) cultured under sparse (SPG) and confluent (CFG) conditions. The upper and lower AFM images represent cell surface topography and elastic modulus map, respectively. Results of the surface elastic modulus show at the nucleus region ((I), (K)) and at cell body ((J), (L)). The red arrowheads in (G) indicate a linear distribution with a higher elastic value. In the CFG, cell stiffening was observed only in NIH3T3 cells ((I), (J)) but not in HeLa cells ((K), (L)). Mean + SD. n = number of analyzed cells.

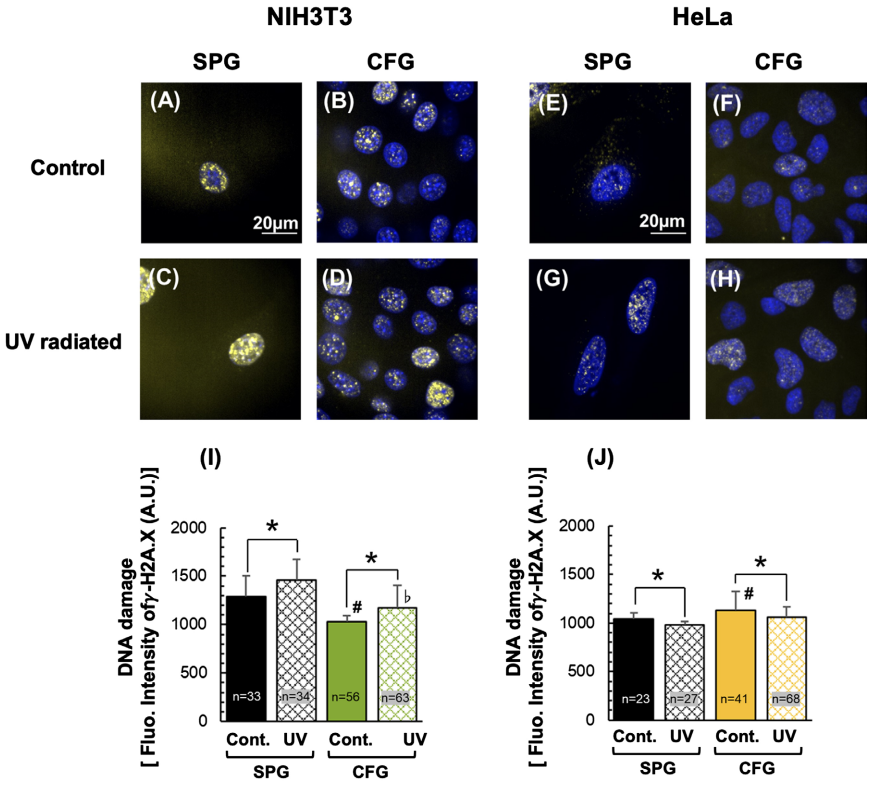

Figure 5. Typical examples of fluorescent images of DNA (blue) and γ-H2A.X (yellow foci) of NIH3T3 ((A)-(D)) and HeLa cells ((E)-(H)). The upper and lower images represent untreated control cells and UV-radiated cells, respectively. Differences in fluorescent intensity of γ-H2A.X in NIH3T3 (I) and HeLa cells (J) cultured under sparse (SPG) and confluent (CFG) conditions. Cont.: untreated control cells. UV: UV-radiated cells. Mean + SD. n = number of analyzed cells. (*): $P < 0.05$. (#): $P < 0.05$, Cont-CFG vs. Cont-SPG. In the untreated control state, DNA damage in NIH3T3 cells significantly decreased with cell crowding (I) but increased in HeLa cells cell crowding (J). UV radiation-induced DNA damage was clearly observed in NIH3T3 cells (I) but not in HeLa cells (J).

4. Discussion

First, we discuss the changes in cell structure, mechanical properties, and endogenous DNA damage caused by cell crowding in NIH3T3 cells. Actin filaments located at the cell periphery in sparse NIH3T3 cells (**Figure 2(A)**) transformed into thick bundles of stress fibers in the cell body surrounding the nucleus following cell crowding with confluency (**Figure 2(C)**), and the surface stiffness increased significantly, especially in the cell body (**Figure 4(I)**, **Figure 4(J)**). Such changes in cell crowding caused nuclear downsizing (**Figure 3(A)**, **Figure 3(B)**) and endogenous DNA damage reduction (**Figure 5(I)**, compare black and green bars), which may have been caused by mechanical stabilization of the nuclei due to the reinforced actin stress fibers around the nuclei (**Figure 2(C)**). The surface elastic modulus of cells depends on the mechanical tension of actin stress fibers [17], which increases with the maturation of cell-cell connections [18]. Furthermore, contact inhibition caused by enhanced cell-cell connections delays the cell cycle [19] [20]. Considering these previous studies and the results of our study, it is

possible that cell crowding in NIH3T3 cells provokes a significant decrease in DNA damage by nuclear downsizing due to the stress fiber-induced mechanical stabilization of the nuclei and cell cycle delay, which causes a decrease in DNA replication frequency.

In contrast, in HeLa cells, partial depolymerization of actin filaments was observed with cell crowding (**Figure 2(D)**) and cell surface stiffness did not increase and it tended to decrease (**Figure 4(K)**, **Figure 4(L)**). Nuclear downsizing also occurred in HeLa cells (**Figure 3(E)**, **Figure 3(F)**), the degree of which was more pronounced than that in NIH3T3 cells, resulting in a significant increase in DNA accumulation (**Figure 3(H)**). Consequently, endogenous DNA damage increased in HeLa cells (**Figure 5(J)**, compare black and yellow bars). Although it is unclear why nuclear downsizing, DNA accumulation, and endogenous DNA damage occurred despite HeLa cell softening with cell crowding, a mechanism specific to cancer cells that is different from that of normal skin fibroblasts may be involved. Loss of contact inhibition is a hallmark of cancer cells, and yes-associated protein, a transcriptional regulator that induces cell proliferation, is localized in the nucleus of cancer cells [21]. Therefore, HeLa cells proliferate continuously even at confluency and push against each other, causing cell-cell mechanical stress and resulting in the disruption of actin filaments and cell softening. This reduces their role in protecting the nucleus from external forces, and may induce excessive mechanical stress in the nucleus and endogenous DNA damage.

We also examined the changes in UV-induced DNA damage in cells. The expression of γ-H2A.X increased after UV radiation of NIH3T3 cells regardless of the cell density (**Figure 5(I)**), suggesting that the cell crowding of NIH3T3 cells did not suppress UV-induced DNA damage. The crowding of NIH3T3 cells, in this study, did not induce DNA accumulation (**Figure 3(D)**). Nagayama *et al.* [8] demonstrated that UV-induced DNA damage was effectively suppressed by significant deformation of the cell nucleus using a substrate with an array of micropillars, which also induced the accumulation of intranuclear DNA. Thus, accumulation of intranuclear DNA is also a key factor in suppressing UV-induced DNA damage in NIH3T3 cells.

In contrast, the expression of γ-H2A.X did not increase after UV radiation of HeLa cells (**Figure 5(J)**). Cancer cells are less sensitive to UV than normal cells [22]. These results suggest that the UV radiation intensity used in this study was relatively weak and may not have resulted in UV-induced DNA damage in HeLa cells.

Our study had some limitations. The influence of the cell cycle was not considered. This may result in a large variation in the fluorescence intensity of γ-H2A.X. Although we succeeded in quantitatively analyzing the expression of γ-H2A.X (**Figure 1**), because the DNA damage repair processes of cells are strongly dependent on the cell cycle [23], cell cycle effects should be considered in future studies. The formation of cyclobutane pyrimidine dimers (CPDs) with conformational changes in DNA base pairs also occurs following UV radiation [24] [25]. Future studies should evaluate UV-induced CPDs in addition to DNA double-strand breaks.

5. Conclusion

In this study, the effects of cell density on the mechanical environment of the cell nucleus and cellular DNA damage resistance were investigated in NIH3T3 and HeLa cells, focusing on their in-tracellular structures and mechanical properties. Cell crowding in NIH3T3 cells induced reinforcement of actin filament structures, cell stiffening, and nuclear downsizing, resulting in a significant decrease in endogenous DNA damage. In contrast, crowding in HeLa cells caused partial depolymerization of actin filaments and cell softening, inducing endogenous DNA damage. UV radiation of NIH3T3 cells significantly increased DNA damage; however, the response did not change with cell crowding. In contrast, UV radiation to HeLa cells did not increase DNA damage in either the sparse or confluent state. These results suggested that cell crowding significantly influenced endogenous DNA damage in cells and was quite different in NIH3T3 and HeLa cells. However, cell crowding did not affect the UV-induced DNA damage in either cell type.

Acknowledgements

This work was supported in part by a Grant-in-Aid from the Ministry of Education, Culture, Sports, Science, and Technology, Japan (nos. 21H03804, 22K19890, and 24K03246).

Conflicts of Interest

The authors declare no conflicts of interest regarding the publication of this paper.

References

[1] Paschke, R. (2011) Molecular Pathogenesis of Nodular Goiter. *Langenbeck's Archives of Surgery*, **396**, 1127-1136. https://doi.org/10.1007/s00423-011-0788-5

[2] Someya, M., Hasegawa, T., Nakamura, A.J., Tsuchiya, T., Kitagawa, M., Gocho, T., *et al.* (2023) Prediction of Late Adverse Events in Pelvic Cancer Patients Receiving Definitive Radiotherapy Using Radiation-Induced γ-H2AX Foci Assay. *Journal of Radiation Research*, **64**, 948-953. https://doi.org/10.1093/jrr/rrad079

[3] Nakamura, A.J. (2021) Beyond Visualization of DNA Double-Strand Breaks after Radiation Exposure. *International Journal of Radiation Biology*, **98**, 522-527. https://doi.org/10.1080/09553002.2021.1930268

[4] Takata, H., Hanafusa, T., Mori, T., Shimura, M., Iida, Y., Ishikawa, K., *et al.* (2013) Chromatin Compaction Protects Genomic DNA from Radiation Damage. *PLOS ONE*, **8**, e75622. https://doi.org/10.1371/journal.pone.0075622

[5] Shah, P., Hobson, C.M., Cheng, S., Colville, M.J., Paszek, M.J., Superfine, R., *et al.* (2021) Nuclear Deformation Causes DNA Damage by Increasing Replication Stress. *Current Biology*, **31**, 753-765.e6. https://doi.org/10.1016/j.cub.2020.11.037

[6] Nagayama, K. and Fukuei, T. (2019) Cyclic Stretch-Induced Mechanical Stress to the Cell Nucleus Inhibits Ultraviolet Radiation-Induced DNA Damage. *Biomechanics and Modeling in Mechanobiology*, **19**, 493-504. https://doi.org/10.1007/s10237-019-01224-3

[7] Nagayama, K., Hamaji, Y., Sato, Y. and Matsumoto, T. (2015) Mechanical Trapping of the Nucleus on Micropillared Surfaces Inhibits the Proliferation of Vascular

Smooth Muscle Cells but Not Cervical Cancer Hela Cells. *Journal of Biomechanics*, **48**, 1796-1803. https://doi.org/10.1016/j.jbiomech.2015.05.004

[8] Nagayama, K., Sagawa, C. and Sato, A. (2023) Deformation and Trapping of Cell Nucleus Using Micropillar Substrates Possibly Affect UV Radiation Resistance of DNA. *Journal of Robotics and Mechatronics*, **35**, 1158-1164. https://doi.org/10.20965/jrm.2023.p1158

[9] McBride, S.H. and Knothe Tate, M.L. (2008) Modulation of Stem Cell Shape and Fate A: The Role of Density and Seeding Protocol on Nucleus Shape and Gene Expression. *Tissue Engineering Part A*, **14**, 1561-1572. https://doi.org/10.1089/ten.tea.2008.0112

[10] Shah, B.S. and Chahine, N.O. (2018) Dynamic Hydrostatic Pressure Regulates Nucleus Pulposus Phenotypic Expression and Metabolism in a Cell Density-Dependent Manner. *Journal of Biomechanical Engineering*, **140**, Article ID: 021003. https://doi.org/10.1115/1.4038758

[11] Doolin, M.T., Smith, I.M. and Stroka, K.M. (2021) Fibroblast to Myofibroblast Transition Is Enhanced by Increased Cell Density. *Molecular Biology of the Cell*, **32**, ar41. https://doi.org/10.1091/mbc.e20-08-0536

[12] Vadla, R., Chatterjee, N. and Haldar, D. (2020) Cellular Environment Controls the Dynamics of Histone H3 Lysine 56 Acetylation in Response to DNA Damage in Mammalian Cells. *Journal of Biosciences*, **45**, Article No. 19. https://doi.org/10.1007/s12038-019-9986-z

[13] Oram, S.W., Liu, X.X., Lee, T., Chan, W. and Lau, Y.C. (2006) TSPY Potentiates Cell Proliferation and Tumorigenesis by Promoting Cell Cycle Progression in Hela and NIH3T3 Cells. *BMC Cancer*, **6**, Article No. 154. https://doi.org/10.1186/1471-2407-6-154

[14] Mattos dos Santos, P.C., Feuser, P.E., Cardoso, P.B., Steiner, B.T., Córneo, E.d.S., Scussel, R., *et al.* (2018) Evaluation of *in Vitro* Cytotoxicity of Superparamagnetic Poly(Thioether-Ester) Nanoparticles on Erythrocytes, Non-Tumor (NIH3T3), Tumor (HeLa) Cells and Hyperthermia Studies. *Journal of Biomaterials Science, Polymer Edition*, **29**, 1935-1948. https://doi.org/10.1080/09205063.2018.1564134

[15] Paddillaya, N., Ingale, K., Gaikwad, C., Saini, D.K., Pullarkat, P., Kondaiah, P., *et al.* (2022) Cell Adhesion Strength and Tractions Are Mechano-Diagnostic Features of Cellular Invasiveness. *Soft Matter*, **18**, 4378-4388. https://doi.org/10.1039/d2sm00015f

[16] An, J., Huang, Y., Xu, Q., Zhou, L., Shang, Z., Huang, B., *et al.* (2010) DNA-PKcs Plays a Dominant Role in the Regulation of H2AX Phosphorylation in Response to DNA Damage and Cell Cycle Progression. *BMC Molecular Biology*, **11**, Article No. 18. https://doi.org/10.1186/1471-2199-11-18

[17] Lu, L., Oswald, S.J., Ngu, H. and Yin, F.C. (2008) Mechanical Properties of Actin Stress Fibers in Living Cells. *Biophysical Journal*, **95**, 6060-6071. https://doi.org/10.1529/biophysj.108.133462

[18] Harris, A.R., Daeden, A. and Charras, G.T. (2014) Formation of Adherens Junctions Leads to the Emergence of a Tissue-Level Tension in Epithelial Monolayers. *Journal of Cell Science*, **127**, 2507-2517. https://doi.org/10.1242/jcs.142349

[19] Leontieva, O.V., Demidenko, Z.N. and Blagosklonny, M.V. (2014) Contact Inhibition and High Cell Density Deactivate the Mammalian Target of Rapamycin Pathway, Thus Suppressing the Senescence Program. *P Proceedings of the National Academy of Sciences of the United States of America*, **111**, 8832-8837. https://doi.org/10.1073/pnas.1405723111

[20] Pavel, M., Renna, M., Park, S.J., Menzies, F.M., Ricketts, T., Füllgrabe, J., *et al.* (2018)

Contact Inhibition Controls Cell Survival and Proliferation via YAP/TAZ-Autophagy Axis. *Nature Communications*, **9**, Article No. 2961. https://doi.org/10.1038/s41467-018-05388-x

[21] Zhao, B., Wei, X., Li, W., Udan, R.S., Yang, Q., Kim, J., *et al.* (2007) Inactivation of YAP Oncoprotein by the Hippo Pathway Is Involved in Cell Contact Inhibition and Tissue Growth Control. *Genes & Development*, **21**, 2747-2761. https://doi.org/10.1101/gad.1602907

[22] Sun, N., Kamarajan, P., Huang, H. and Chao, C.C (2002) Restoration of UV Sensitivity in UV-Resistant Hela Cells by Antisense-Mediated Depletion of Damaged DNA-binding Protein 2 (DDB2). *FEBS Letters*, **512**, 168-172. https://doi.org/10.1016/s0014-5793(02)02250-0

[23] Ambrosio, S., Di Palo, G., Napolitano, G., Amente, S., Dellino, G.I., Faretta, M., *et al.* (2015) Cell Cycle-Dependent Resolution of DNA Double-Strand Breaks. *Oncotarget*, **7**, 4949-4960. https://doi.org/10.18632/oncotarget.6644

[24] Besaratinia, A., Yoon, J., Schroeder, C., Bradforth, S.E., Cockburn, M. and Pfeifer, G.P. (2011) Wavelength Dependence of Ultraviolet Radiation-Induced DNA Damage as Determined by Laser Irradiation Suggests That Cyclobutane Pyrimidine Dimers Are the Principal DNA Lesions Produced by Terrestrial Sunlight. *The FASEB Journal*, **25**, 3079-3091. https://doi.org/10.1096/fj.11-187336

[25] Knips, A. and Zacharias, M. (2017) Both DNA Global Deformation and Repair Enzyme Contacts Mediate Flipping of Thymine Dimer Damage. *Scientific Reports*, **7**, Article No. 41324. https://doi.org/10.1038/srep41324